Controlling deformation in Al/Ti: How interface roughness and rotation drive bimetal mechanics

Avanish Mishra, [1,*] John S. Carpenter, [2] and Saryu J. Fensin [3]
[1] *Theoretical Division, Los Alamos National Laboratory, Los Alamos, New Mexico 87545, USA*
[2] *Sigma Division, Los Alamos National Laboratory, Los Alamos, New Mexico 87545, USA*
[3] *Materials Physics and Applications Division, Los Alamos National Laboratory, Los Alamos, New Mexico 87544, USA*

(Received 22 January 2026; accepted 15 May 2026; published 8 June 2026)

The microstructural characteristics and morphology of interfaces in metals can be crucial in governing the initiation of plasticity and early deformation mechanisms under extreme conditions. During high-strain-rate deformation, these interfaces significantly affect dislocation nucleation, twinning, and other mechanisms that directly impact material strength and failure. Despite their importance, a substantial knowledge gap remains between the observed macroscopic material behavior and the underlying role of bimetal interfaces in plasticity initiation. To address this gap, large-scale molecular dynamics simulations are performed on Al/Ti bimetal structures to examine the effect of interface characteristics on the onset of plasticity under uniaxial compression. Specifically, this study investigates how interface roughness (flat vs waveform interfaces) modifies the initiation of plastic events in the microstructure. Atomistic simulations indicate that interface roughness (a microscopic behavior) reduces the stress required for dislocation nucleation, thereby reducing the peak stress relative to a flat interface. For the square interface, the step height strongly influences plasticity initiation by setting the separation of locally flat regions. Varying the interface rotation relative to the loading direction (macroscopic behavior) reveals that the peak stress for both flat and waveform interfaces initially decreases and then increases with rotation, accompanied by a shift in dominant mechanisms—from Al twinning (flat) to interface sliding and Ti-dominated phase transformation and twinning at lower angles. The change in the stress-strain slope during initial compression reflects how rotation alters the resolved shear stress and activates different slip systems. Overall, the study provides valuable insights into the role of bimetal interfaces in controlling plasticity initiation and early deformation pathways for Al/Ti under extreme loading conditions.

DOI: 10.1103/44bt-jb3p

I. INTRODUCTION

Multiphase metallic materials are promising candidates for structural applications due to their extraordinary properties, such as resistance to corrosion, high strength, thermal stability, remarkable durability, and hardness [1,2]. The improved performance of these multiphase materials is due to the distribution of bimetal interfaces and their ability to control deformation behavior for targeted applications [3,4]. The perusal of the recent literature shows extensive research on how interfaces influence material properties [5]. This involves understanding the impact of low- and high-misorientation grain boundaries, as well as bimetal interfaces with well-defined orientation relationships (ORs) [6,7]. Interface chemistry, interdiffusion, and solutes can also modify the response of bimetals [8,9]. Studies on special grain boundary types—such as twin boundaries in single-phase metals—have also provided important insights into how interface structure affects mechanical behavior. In bimetallic systems, however, most studies primarily examine laminate microstructures with flat and idealized interfaces [6,10,11], often with an emphasis on fcc/bcc microstructures such as Cu/Fe [6], Cu/Ta [12], Cu/W [13], and Cu/Nb [2]. These systems are typically characterized by specific ORs that result in distinct microstructural features, which in turn influence the mechanical response of the composite material. The interaction of the dominant deformation mechanisms, such as dislocation slip and twinning, with interface structure, has been shown to significantly affect overall material behavior [11,14]. For example, studies on Cu/Ta interfaces reveal that the ORs control dislocation slip and twinning behavior, consequently modifying deformation and failure mechanisms [15]. Similarly, in Cu/Fe, the presence of the interface modifies the phase variants observed in Fe during compression, thereby altering the types of twins formed upon stress relaxation and the overall response of the bimetals [6,16,17].

Despite significant progress, several critical knowledge gaps remain. Most prior studies have focused on atomically flat Kurdjumov-Sachs (KS) interfaces or on faceted ORs such as KS112 in fcc/bcc bimetals [11,18–20]. Studies on Cu/Nb with KS112 interfaces show that faceted interfaces support twinning due to associated misfit dislocations [20]. Under compressive loading, deformation at atomically sharp KS interfaces in physical vapor deposition (PVD)-synthesized Cu/Nb is controlled by dislocation motion [21,22]. In contrast, accumulative roll-bonded (ARB) Cu/Nb has faceted KS112 interfaces [22]. These structural differences produce distinct mechanical behavior, with KS112 interfaces exhibiting enhanced yield strength and flow stress under uniaxial

*Contact author: avanish@lanl.gov

compression. However, the interfaces found in real materials are rarely perfectly flat or ideally faceted; they are often rough, irregular, and contain local deviations in orientation and structure. Regions with locally modified ORs or topographic irregularities can significantly influence deformation mechanisms [15]. A recent study on serrated interface geometry shows that it affects deformation twinning in Cu/Nb [11]. The effect of interfacial roughness on the mechanical response remains largely unexplored, even though it can significantly influence dislocation behavior, twinning, and overall deformation mechanisms. This gap is one of the reasons for the mismatch between modeling and experimental observations under high strain-rate loading. Therefore, to bridge this gap, it is essential to systematically investigate the mechanical response of rough interfaces in bimetallic systems.

Furthermore, current research predominantly focuses on fcc/bcc interfaces [8,9,11], while research involving hexagonal close-packed (hcp) metals—such as titanium (Ti)—is limited [23–27]. The hcp structure introduces additional anisotropy and complex deformation mechanisms that could significantly influence interface behavior under high strain-rate loading. A recent molecular dynamics (MD) study explored the role of interfaces in a Ti alloy, showing that interfaces localize tensile stress and nucleate multiple voids [28]. Previous work on hcp/fcc bimetals has demonstrated that ORs play a critical role in crack initiation and propagation during dynamic deformation [24]. Additionally, the response of bimetals also varies with the orientation of the interface relative to the loading direction [22,29]. For instance, in Cu/Ta bimetals, loading perpendicular versus parallel relative to the interface modifies the activation of slip systems in the microstructures [30]. Rotation can lead to transitions between migration, sliding, and different slip systems [29]. This is particularly noteworthy, as interfaces may also rotate under dynamic loading conditions. These gaps underscore the importance of understanding how crystal structure, interface roughness, and inclined or evolving interfaces influence the deformation mechanisms of bimetal microstructures—especially for Al/Ti and related systems.

The modification in the material response due to interfaces also suggests an exciting prospect: By deliberately engineering interface structures—from flat to rough or inclined—it is possible to design materials for targeted applications. Experiments have shown that even flat interfaces with fixed ORs can be tailored to alter material behavior by controlling processing conditions [31]. However, conducting experiments to systematically study these factors (interface geometry, roughness, and rotation) under high strain-rate conditions is often arduous. Large-scale MD simulations offer a promising solution for examining material response under high-rate deformation [10,32–37]. In addition to providing insight into dynamic deformation, atomistic simulations guide experiments by systematically exploring engineering variables, including interface spacing, roughness, and interface type, that govern the high-rate deformation response of bimetals. For example, MD simulations have helped unravel the reason behind the different responses of Cu/Nb bimetals manufactured by PVD and ARB methods [2] and have clarified modifications in twins and phase-transformation variants in Fe during deformation [6]. Given their ability to capture atomic-scale interactions and resolve transient phenomena, MD simulations are well suited to address the knowledge gaps outlined above, including those related to crystal structure, interface roughness, and orientation-dependent response in bimetallic materials under high strain-rate loading.

Herein, MD simulations are used to understand the response of a bimetal material involving an fcc/hcp interface under strain-controlled uniaxial compression tests. Specifically, Al/Ti bimetals with the Shoji–Nishiyama (SN) orientation relationship [38] are used in this study. The excellent strength and corrosion resistance of Ti and the ductility of Al have attracted interest in designing lightweight materials for the automotive, aerospace, and defense industries [39,40]. It is shown that interface-mediated plasticity and variant selection are active in Ti alloys [41–43]. Next, to examine the role of interface roughness during the deformation of the bimetal with an SN interface, a generalized method to generate various waveform interfaces is proposed. The simulation results show that waveform interfaces (i.e., interface roughness) ease dislocation nucleation, thereby modifying the initiation of plasticity and the early deformation mechanisms. Finally, the role of interface rotation is examined, establishing that the response and deformation mechanisms change as the interface is rotated with respect to the loading direction. Additionally, interface roughness (waveform interfaces), when combined with interface rotation, further influences the response of inclined interfaces, reducing the peak stress.

This paper is organized as follows: Section II presents computational details, deformation conditions, and microstructure characterization methods; Sec. III describes the results; and the conclusion provides a brief summary and discussion. This work isolates how interface roughness and interface rotation, independently and jointly, control dislocation nucleation stress, peak stress, and twinning, sliding, and phase transformation in Al/Ti under high-rate compression. This study focuses on the effect of interface roughness on qualitative, local mechanism trends at high strain rate rather than achieving one-to-one agreement with experimental interface roughness.

II. COMPUTATIONAL DETAILS

A. Simulation setup

MD simulations are performed using the Large-scale Atomic/Molecular Massively Parallel Simulator (LAMMPS) [44]. The interaction between Al and Ti atoms is represented using the Embedded Atom Method (EAM) potential developed by Zope and Mishin [45]. This potential has been used to understand the deformation behavior and alloying in the Al/Ti system [28,41,46,47]. The EAM potential reproduces the structural and thermodynamic properties of Al and Ti with good overall accuracy. For Al, the lattice constant matches experiment exactly, whereas stacking-fault energies deviate by $\sim$4%. For Ti, the lattice constants agree within 0.2%; however, stacking fault deviates. The EAM potential underestimates the basal intrinsic stacking-fault energy in Ti relative to experimental estimates, which can promote stacking-fault formation and may lower the onset of predicted twinning stress/strain. Therefore, twinning/stacking-fault stress/strain

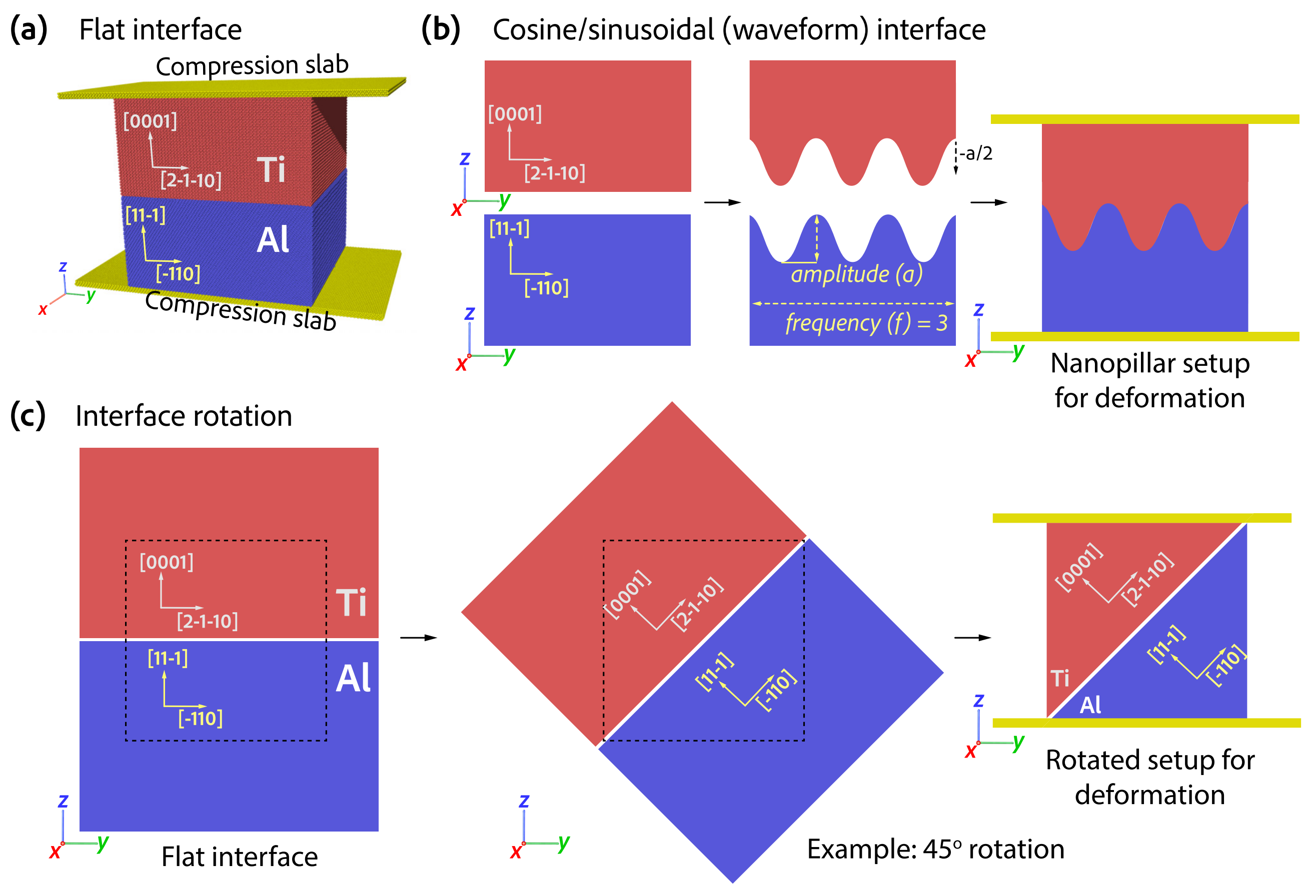

FIG. 1. (a) Al/Ti bimetal interface with the SN orientation relationship, (b) steps used to construct a cosine (waveform) interface, and (c) procedure used to rotate the interface relative to the loading direction. An example of rotating the flat interface to 45° is shown; a similar approach is used for the waveform interfaces.

should be interpreted qualitatively and emphasis should be made on comparing the trends across interfaces since the same potential and loading conditions are considered. Consistent with first-principles calculations, the EAM potential predicts that the fcc Ti phase is higher in energy than the hcp phase by ∼0.011 eV/atom; thus, it is suitable for capturing any hcp to fcc transformation under extreme local stress states. This potential is used here for a comparative study, and although its absolute values may differ slightly from experiment or other interatomic potentials, the overall trends and relative behaviors are expected to remain consistent. The simulation cell size is $\sim30 \times \sim30 \times \sim30\,\mathrm{nm}^3$(∼2 million atoms), comprising Al and Ti regions of $\sim30 \times \sim30 \times \sim15\,\mathrm{nm}^3$ each, joined at a midplane interface with an SN OR. This size was chosen to reduce the strain between Al and Ti to ∼0.2% in the X−Y interface plane due to lattice mismatch between the two materials.

Uniaxial compression is performed using a nanopillar setup, as shown in Fig. 1(a). The simulation cell also contains two compression slabs located at the top and bottom, as shown in Fig. 1(a). The Al/Ti bimetal interface is periodic only along the X direction (the simulation cell is periodic in X and nonperiodic in Y and Z; no vacuum is added). Moreover, because the samples are rotated later about the X axis to examine the role of interface rotation, enforcing periodicity along Y would introduce a geometric discontinuity of the interface across periodic images. Therefore, we retain periodicity only along the interface-extended direction (X) and use a free boundary in Y to avoid nonphysical mismatch. Hence, throughout the study the simulations are nonperiodic in the Y direction and include free surfaces in that direction. The compression slabs are included solely to examine the role of interface morphology in the mechanical response and to prevent periodic-image interactions between Al and Ti along the Z direction (thereby avoiding formation of a second interface). Before loading, all simulation cells are equilibrated in an NPT ensemble (Nosé–Hoover thermostat/barostat) at 300 K for 120 ps with a time step of 2 fs. The evolution of the potential energy, kinetic energy, pressure, and stress components during equilibration is shown in Fig. S1 [48]. The strain-controlled uniaxial compression is performed at a $10^8\,\mathrm{s}^{-1}$ strain rate by loading along the Z direction, while barostatting the X direction to $\sigma_x = 0$ at 300 K (i.e., zero average stress along the X direction) and measuring σ_z. The applied strain rate here is significantly higher than experimental rates (10^3–$10^6\,\mathrm{s}^{-1}$); however, it is sufficient to capture the qualitative deformation trends rather than the absolute yield values. The discussion about stress calculation via cuboid tracing (Fig. S2 [48]) and microstructure characterization is discussed in Supplemental Material [48]. The atomistic microstructure considered here does not replicate experimental length scales; however, the goal of this study is not to replicate experimental findings but to examine how interface roughness and orientation modify the bimetal response. All atomistic configurations were visualized and analyzed using the Open Visualization Tool (OVITO) [49].

B. Interface setup

1. Interface roughness

The OR for fcc/hcp (Al/Ti) considered here is the SN [38] that involves $(11\bar{1})$fcc ∥ (0001)hcp and $[1\bar{1}0]$fcc∥$[21\bar{1}0]$hcp relationships. The SN OR generates a flat interface without faceting, which serves as a baseline for later comparison. The goal is to choose a reported OR, often found in experiments, and create a waveform morphology at the interface. The interface morphology was modified to a waveform to capture changes in interface shape associated with the bonding/manufacturing method. Here, the waveform morphology is representative of interfaces produced by explosion bonding. The approach for creating the interface roughness involves selecting a waveform pattern at the top of the lower metal (Al) and an opposite pattern at the bottom of the upper metal (Ti), as shown in Fig. 1(b). The atoms below (Al) and above (Ti) the defined patterns are used to construct a bimetal interface that has a waveform morphology. To align the crests of the Al surface with the troughs of the Ti surface, the upper metal (Ti) is shifted downward by half the amplitude of the waveform pattern when forming the interface. The following selection criteria create a cosine/sinusoidal interface. For Al (the lower metal), the atoms satisfying the following Z-coordinate conditions are selected:

$$z_{\mathrm{Al}} < z_{\max} + a\left[\cos\left(\frac{2\pi f y}{y_{\max}} + s\right) + 1\right]. \tag{1}$$

For Ti (the upper metal), the atoms satisfying the following Z-coordinate condition are selected:

$$z_{\mathrm{Ti}} > a\left[\cos\left(\frac{2\pi f y}{y_{\max}} + s\right) + 1\right]. \tag{2}$$

Here, y and z are the Y and Z coordinates, $y_{\max}$ and $z_{\max}$ are the maximum values of Y and Z for the respective metals (with $z_{\max}$ referring to Al). a and f are the desired amplitude and frequency for the cosine wave, and s is the phase shift (set to $s = 0$ in this study). A nonzero s can be used to introduce notches at the interface or to create a mixed interface. It should be noted that both metals initially have the origin at (0, 0, 0). A Python code is developed to generate different waveform interfaces using similar equations for the other waveform morphologies. The code can create interfaces with morphologies such as cosine/sinusoidal, sawtooth, square, pulse, or even noisy (provided a mathematical expression is defined). The amplitude and frequency of these waveform interfaces can be provided as an input. These interfaces are periodic along the Y and X directions; the number of cycles is set by f. However, the Y-direction periodicity is removed during deformation simulation. Cosine, sawtooth, and square waveform interfaces are considered for simulation, as shown in Fig. S3 [48]. This approach involves modifying only the morphology at the interface while keeping the overall orientation between the bimetals the same. Therefore, it highlights changes in microscopic degrees of freedom, and the bulk Schmid factors remain unchanged because the crystallographic OR is fixed. The frequency for these waveform interfaces is fixed at 3. The amplitude and frequency considered here correspond to typical roughness scales observed in explosion-bonded Al/Ti [50] and are used as example cases to demonstrate the role of roughness; these parameters can be varied for a more detailed analysis. These interfaces are simplified surrogates for process-induced interfacial waviness and steplike roughness rather than exact replicas of experimentally observed interfaces. This allows us to examine the role of interface roughness independently of any changes in the orientation relationship.

2. Interface rotation

Further, to investigate the role of interface rotation with respect to the loading direction, we rotate flat and cosine-wave interface microstructures to different angles relative to the loading direction, as shown in Fig. 1(c). The rotation is performed about the periodic X axis by applying a rotation matrix to the bimetal coordinates. First, the bimetal with a flat or cosine-wave interface is rotated to the desired angle. Next, a portion of this rotated structure is cropped to create the nanopillar setup, ensuring a region of approximately 30 nm (along the loading direction) is maintained between the upper and lower compression slabs. To avoid any orientation mismatch, we crop the compression slabs directly from the rotated sample rather than using preexisting slabs with a fixed orientation. This approach ensures that the slab crystal orientations are aligned with the adjacent metals, thereby avoiding artificial rotation during deformation that would obscure the isolated effect of interface orientation on deformation mechanisms [40]. The microstructure is rotated in 10° increments, from 0° to 90°, with an additional case at 45°. This rotation changes the Schmid factors of the metals, thereby modifying the macroscopic degrees of freedom. These rotated microstructures represent inclined interfaces that can form due to joining geometry or local interface reorientation during deformation. This allows us to examine the role of interface rotation with respect to the loading direction.

III. RESULTS AND DISCUSSION

A. Flat interface

First, the flat interface with the SN OR is deformed at a strain rate of $10^8\ \mathrm{s}^{-1}$. The stress-strain curve for the Al/Ti flat SN interface under uniaxial compression at a $10^8\ \mathrm{s}^{-1}$ strain rate is shown in Fig. 2(a). The peak compressive stress for the flat interface Al/Ti bimetal (computed by tracking the stress in the cuboid) is 5.81 GPa at a strain of 0.045 (4.5%). The drop after the peak stress is correlated with twinning and dislocation nucleation in Al, as shown in Fig. 2(b). At a similar strain level, dislocations nucleate at the bottom corner of the Al region due to a higher stress concentration between the slab and the nanopillar and propagate toward the interface. In Al, the types of dislocations include Shockley partial dislocations, stair-rod dislocations, and perfect dislocations. A small number of dislocations with a $1/3\langle\bar{1}110\rangle$ Burgers vector are first observed in Ti at approximately the same strain value (4.9%), near the interface. The evolution of different types of dislocations in Al and Ti for flat interfaces is shown in

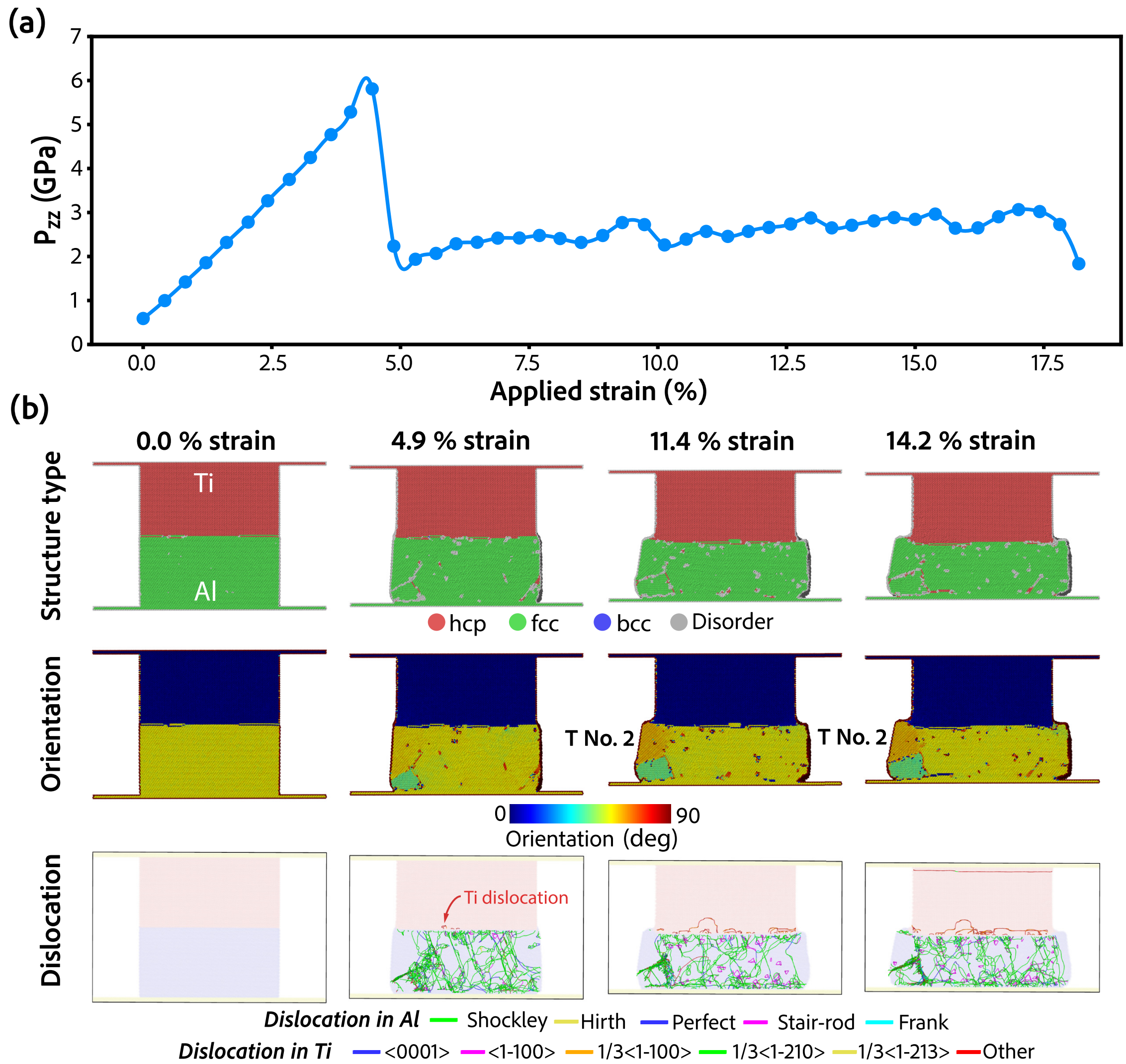

FIG. 2. (a) Stress–strain response for Al/Ti bimetals with a flat interface under uniaxial compression. Scatter points indicate stress values from simulations, and the line is a spline fit. (b) Evolution of structure type, orientation angle, and dislocations in the microstructure at four strain values. Label T No. 2 at 11.4% and 14.2% strain highlights the rotation of Al atoms.

Fig. S4 [48]. Figure 2 also shows that the softer Al deforms more than Ti, as demonstrated by the mushrooming of Al. The calculated atomic shear strain (atomic von Mises shear strain invariant) with respect to the initial structure highlights minimal deformation in Ti, while Al undergoes significant deformation (Fig. S5 [48]). At 11.4% applied strain, deformation in Al produces a localized microscopic rotation of Al atoms, which leads to the nucleation of a twin region. The rotated region [labeled as T No. 2 in Fig. 2(b)] appears at the outer left edge of the bimetal and is observed only on the side where the first twin forms. Thus, at ∼11% strain, the deformation of Al, the nucleation of the first twin region, and increased outer-surface displacement occur together and are accompanied by significant local atomic rotation. In contrast, no twinning is observed in Ti. Additionally, at approximately 14% strain, dislocations are also observed in Ti, specifically at the top near the slab/cell interface (Fig. 2). Overall, the deformation of Al/Ti bimetals with a flat interface results in the onset of plasticity through twinning and dislocation nucleation within Al, along with the mushrooming of the softer Al.

B. Interface roughness

Next, the impact of interface roughness on the deformation mechanisms in Al/Ti bimetal interfaces with cosine, sawtooth, and square morphologies is examined at the same strain rate. For each case, two different amplitudes (30 Å and 60 Å) for the waveform interfaces are considered. The frequency for these waveform interfaces is fixed at 3. The OR for waveform interfaces is based on the initial flat SN OR. The peak stress for bimetals with waveform interfaces is significantly lower than that for the flat interface, as mentioned in Table I. The important point is that, compared to the flat interface, for waveform interfaces, increased interfacial length combined with preexisting dislocations at interfaces reduces the stress required for initiation of plasticity. Additionally, it modifies the initial deformation mechanism from the Al twinning observed in the flat-interface case toward interface-mediated dislocation activity. Thus, in the present nucleation-controlled regime, roughness primarily modifies interfacial activation rather than changing the flow state.

TABLE I. Peak compressive stress (P_{zz}(max)) and strain (ε) at σ_{max} for bimetals with different interface types and amplitudes.

Interface type	Waveform amplitude (Å)	P_{zz}(max) (GPa)	Strain (ε) at P_{zz}(max)
Flat		5.81	4.50%
Cosine	30	3.94	3.22%
	60	3.66	3.62%
Sawtooth	30	3.67	3.22%
	60	3.09	2.20%
Square	30	3.03	1.13%
	60	3.88	3.22%

Compared to the flat interface, for the case of the waveform interfaces with a 60 Å (30 Å) amplitude, the peak stress is reduced by 37.01% (32.18%), 46.82% (36.83%), and 33.22% (47.85%) for the cosine, sawtooth, and square interfaces, respectively. This indicates that modification of interface morphology changes the deformation mechanisms in bimetals, as shown in Fig. 3. Table I lists the peak compressive stresses calculated for the different bimetal waveform interfaces. This change in the mechanical response correlates with an increase in the interface length. For a microstructure with a width of 30 nm along the Y direction, the flat interface length remains 30 nm. However, when considering a cosine interface with amplitudes of 60 Å and 30 Å (frequency of 3) while maintaining the same width, the interface length increases to approximately 80 nm and 49 nm, representing an increase of ∼167% and ∼63%, respectively. An interface is a weak region that facilitates dislocation nucleation; therefore, increasing its length reduces the strength. Increasing both the amplitude and frequency of the waveform interface (especially for the cosine and sawtooth) increases the interface length compared to the flat interface. The difference in response at different amplitudes for the cosine interface is highlighted by the inset in Fig. 3. The increase in peak stress values for cosine and sawtooth interfaces at lower amplitudes (30 Å) can be attributed to a reduced interface length, although the change in strength is not proportional to the change in length (Fig. S6 [48]). Similarly, for sawtooth interfaces with amplitudes of 60 Å and 30 Å, the interface length increases to ∼78 nm (∼160%) and ∼47 nm(∼56%), respectively (Fig. 4). The red arrows in Fig. 4 highlight the geometric features that increase the interface length. The effect of using a periodic Y-direction deformation setup, as well as the role of interface frequency, is discussed in the Supplemental Material (Sec. S7 and Figs. S7 and S8 [48]).

As shown in Fig. 4, for the square interface the total interface length increases to approximately 102 nm (60 Å amplitude) and 66 nm (30 Å amplitude), representing increases of ∼239% and ∼119%, respectively. However, this increase is due to the formation of steps that separate flat, 5 nm-wide interface regions at a fixed height (Fig. 4). Consequently, the interface remains locally flat but is separated by steps. The amplitude-dependent response of the square interface differs from that of the cosine and sawtooth interfaces (Fig. 3, S6, and S9 [48]). Reducing the amplitude decreases the step height from 12 nm to 6 nm, bringing the flat interface regions closer together. For the 60 Å amplitude, the 12 nm vertical separation forms tall pillars that accommodate the initial deformation, delaying dislocation nucleation in Al and

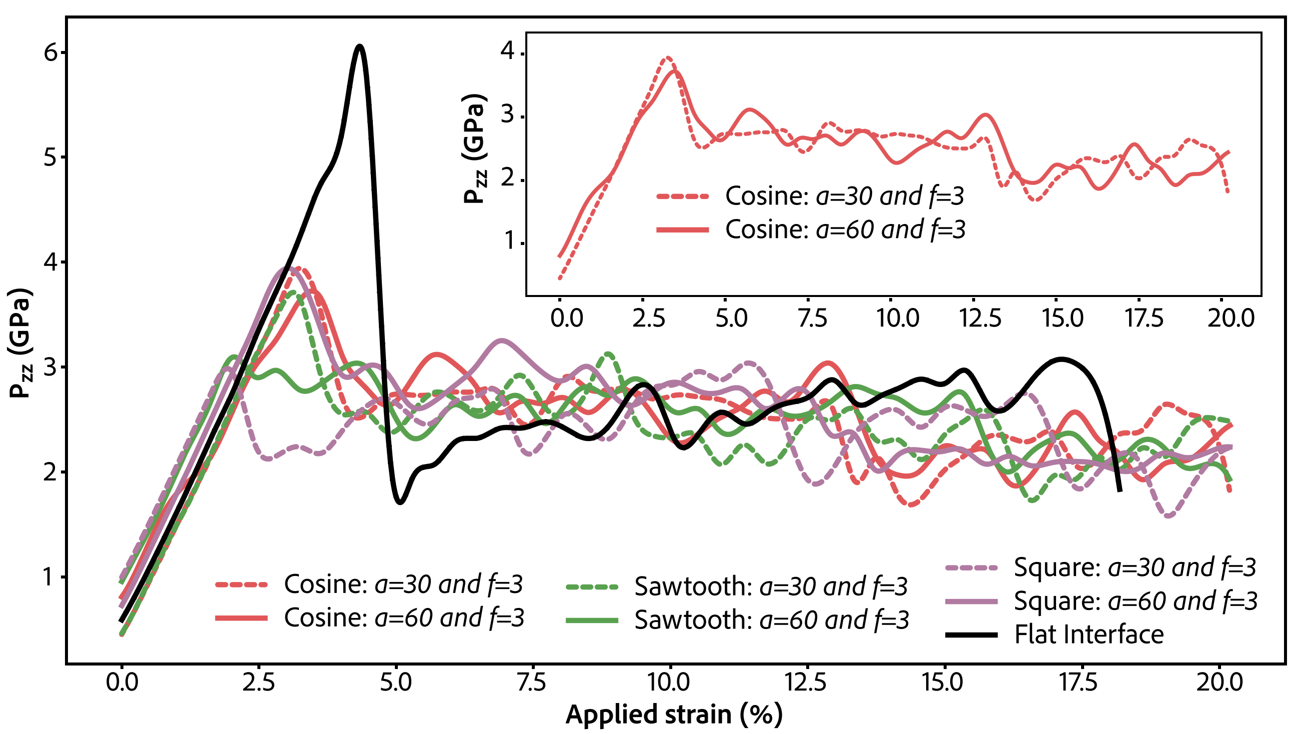

FIG. 3. Stress–strain responses for Al/Ti bimetals with waveform interfaces. The line plots are spline fits to the computed stress. The inset plot shows the stress–strain response for the cosine interface. Figure S6 [48] shows individual stress–strain responses for waveform interfaces at two amplitudes.

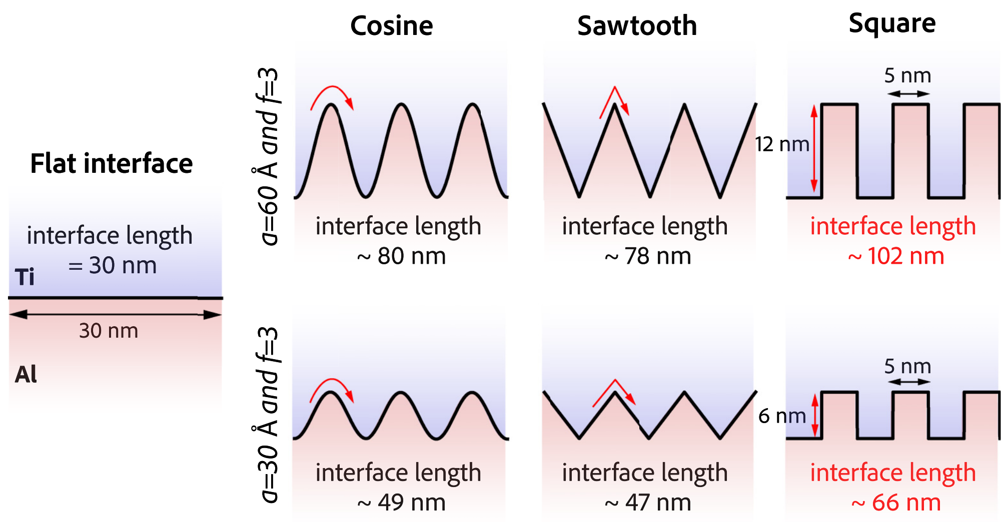

FIG. 4. Interface length for flat and waveform interfaces. Waveform interfaces with two amplitudes (a)—60 Å and 30 Å—at frequency $f = 3$ are considered. Red arrows indicate features that increase the interface length.

increasing the required stress (Fig. S10 [48]). In contrast, for the 30 Å amplitude, the 6 nm pillar height positions the separated regions closer to the Al cell, which eases dislocation nucleation and reduces the required stress (Fig. S10 [48]). Therefore, modifying the microscopic degrees of freedom—i.e., interface roughness from flat to waveform—alters the onset of plasticity and the early deformation response of Al/Ti bimetals. In addition, for the square interface, the step height is an important, experimentally accessible parameter for engineering and controlling bimetal deformation. Across all waveform cases, the common mechanism is the same: roughness weakens the interface-controlled activation barrier for plasticity. The square interface is an exception as total interface length alone does not determine the response; because the interface remains locally flat between vertical steps, the spacing of flat segments and the step height also control how deformation is partitioned and when dislocations nucleate.

Bimetals with a waveform-interface amplitude of 60 Å are examined to identify the mechanisms by which peak stress and strain are reduced relative to a flat interface. It is well established and, as mentioned in Table I, interfaces lower the stress required for dislocation nucleation. Unlike the flat bimetal interface, where no interfacial dislocations are present prior to loading, having a cosine profile inherently introduces dislocations at the interface, primarily on the Al side, as shown in Fig. 5. During deformation, the dislocations in Al glide away from the interface toward the simulation-cell boundary and the fixed compression slab, which is not the case for the flat interface where dislocations had to nucleate first. Notably, these dislocations start moving at a low strain of ∼1.2%, well before the peak compressive stress (3.62%), as shown in Fig. 5. At the same stage, dislocations are also detected in the Ti cell near the interface (troughs of the interface). At approximately 4.03% strain, dislocations remain concentrated in the Al cell; however, within the microstructure they are largely trapped in the interfacial region. These regions correspond to a trough in Ti and a crest in Al at the interface, as shown in Fig. 5. Similar to the flat interface, dislocations are also observed at the compression slab/Ti-cell boundary (top of the cell in Fig. 5) during the late stages of deformation (18.2% strain). No twinning is observed in any waveform-interface bimetal, in contrast to the flat interface where twinning in Al accompanies dislocation activity. The previously noted mushrooming of the softer Al is again observed for waveform interfaces. However, the amount of mushrooming in Al is reduced in these modified morphologies at the same strain (14.2%), as shown in Fig. S11 [48]. This is because more of the imposed deformation is accommodated within the interfacial waveform region. Relative to the flat interface at a similar strain value, the calculated atomic shear strain shows additional deformation within Ti (more shear bands in Ti), particularly at the crests of the interface (Fig. S11 [48]). The applied strain for pronounced mushrooming is increased for the cosine interfaces (∼6% applied strain) compared to the flat case (∼4%). Hence, these observations indicate that in the nucleation-controlled regime considered here, optimizing the amplitude and frequency of rough, cosinelike interface morphologies can reduce the stress required for plasticity initiation and enable bimetals to sustain greater deformation, especially for hard/soft material pairs.

The deformation of the sawtooth interface is similar to that of the cosine interface, although fewer interfacial dislocations are present prior to deformation. In this case, during deformation, dislocations travel away from the interface toward the bottom of the simulation cell, as shown in Fig. S12(a) [48]. Similar to the cosine interface, no twinning is observed. The dislocations at the interface are concentrated at the crests in Al and the troughs in Ti. Furthermore, dislocations accumulate at the bottom of the microstructure. Mushrooming of Al is observed, following the characteristics of the cosine interface and indicating more continuous deformation rather than the discrete steps observed for the flat interface, as shown in Fig. S12(a) [48]. In the case of the square waveform interface, prior to deformation, some dislocations are observed near the vertical steps of the square waveform (within Al), while the horizontal parts of the interface remain free of dislocations, as shown in Fig. S12(b) [48]. The horizontal segments are

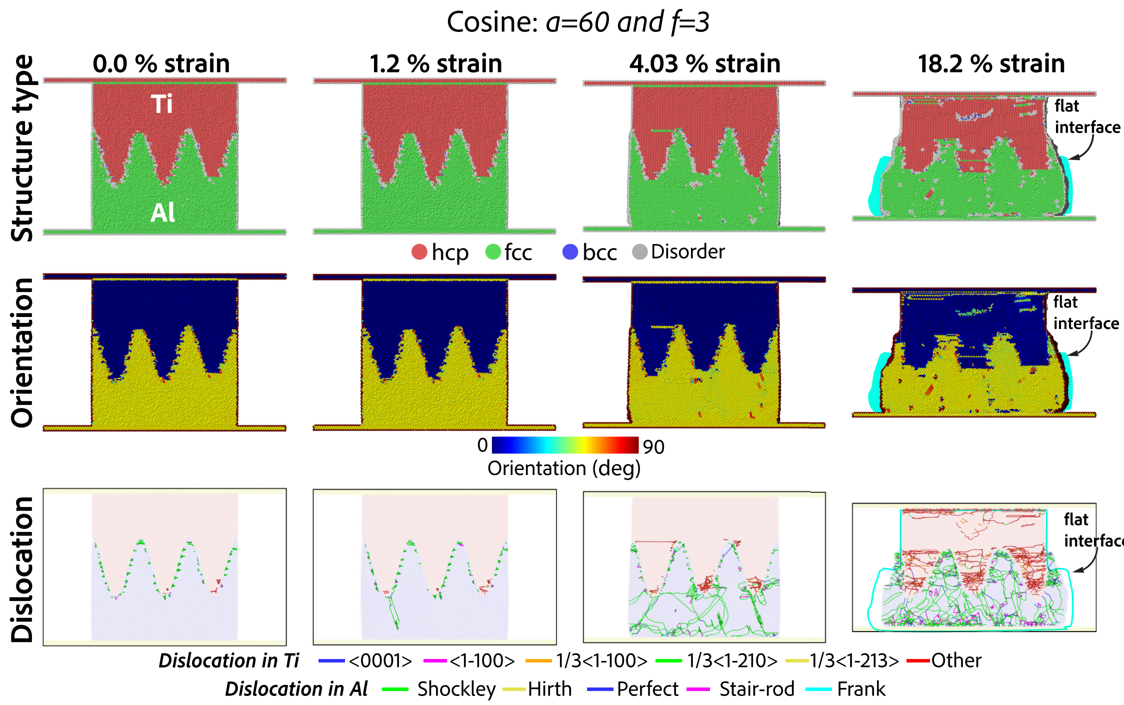

FIG. 5. Evolution of structure type, orientation, and dislocations for bimetal with the cosine interface ($a = 60$ Å and $f = 3$) at four different strain values. The cyan-colored region plotted behind the cosine-interface bimetal indicates the mushrooming observed at the 18.2% strain for the flat-interface case.

similar to the flat interface; hence, no dislocations are observed. With no twinning in these cases during deformation, the reduction in stress is due to dislocation glide, similar to that observed previously for cosine and sawtooth interfaces. Surprisingly, for square waveforms, mushrooming is observed in both Al and Ti. The mushroomed part of Ti is a result of the simulation setup, as one of the Ti pillars is not encapsulated by Al. This causes a $\sim 7^\circ$ change in orientation of that Ti pillar at higher strain, as shown in Fig. S12(b) [48]. If Ti pillars were similarly not encapsulated in the other waveform interfaces, comparable effects would also have been observed. This underscores an approach to controlling the deformation of Ti or other harder materials. In all these cases, the geometry of the interfaces remains almost unchanged during compression. The stress-strain profile and deformation mechanisms remain similar for low-amplitude waveform interfaces compared to the high-amplitude case. In waveform interface cases, dislocations are present at the interface prior to deformation, and no evidence of twinning is observed. Moreover, the evolution of different types of dislocations at waveform interfaces is shown in Fig. S4 [48]. For all cases, Shockley partials are the dominant dislocations in Al; in Ti, the $1/3\langle\bar{1}110\rangle$ and other dislocation densities are dominant and remain close during deformation. Compared with flat interfaces, waveform interfaces show a smaller slope in the increase of dislocation density in both Al and Ti, indicating deformation accommodated at the interface after plasticity is initiated. However, dislocations in Ti appear earlier, and Al always shows some dislocation presence at the interface. This demonstrates that modifications to the structure or interface type, relative to the flat interface, can significantly influence plasticity initiation and deformation characteristics. The microscopic degrees of freedom of the interface control the peak stress and the associated deformation mechanisms, such as twinning and dislocation nucleation and motion, which affect the overall deformation of Al/Ti bimetals.

C. Interface rotation

To examine the effect of interface rotation with respect to the loading direction, the flat interface nanopillar setup described earlier is rotated at various angles and deformed at a strain rate of 10^8 s^{-1}, as shown in Fig. 1(c). The simulation cell for the rotated samples is kept similar to that of the initial flat-interface setup. As the interface is rotated from being perpendicular (90°) to the loading direction, the peak stress first decreases (Fig. 6). This trend is consistent with previous observations [51] that altering the loading direction changes the Schmid factor and the stress required to activate slip systems. With rotation, the peak stress decreases up to about 40° and then increases again, as shown in the inset of Fig. 6. The 45° rotation is an exception, showing a higher peak stress than the 40° and 50° rotations. This deviation is attributed to the specific alignment of the interface with the compression slab, which is discussed later in this section. Minor inconsistencies in peak stress variation at lower angles (at 10°) are attributed to contributions from Ti. Nevertheless, the main point is that the stress–strain response depends on the interface rotation with respect to the loading direction. A similar trend is reported for Cu bicrystals, where the probability of void nucleation is higher when the interface is normal to the loading direction than when it is parallel [51]. The rotation

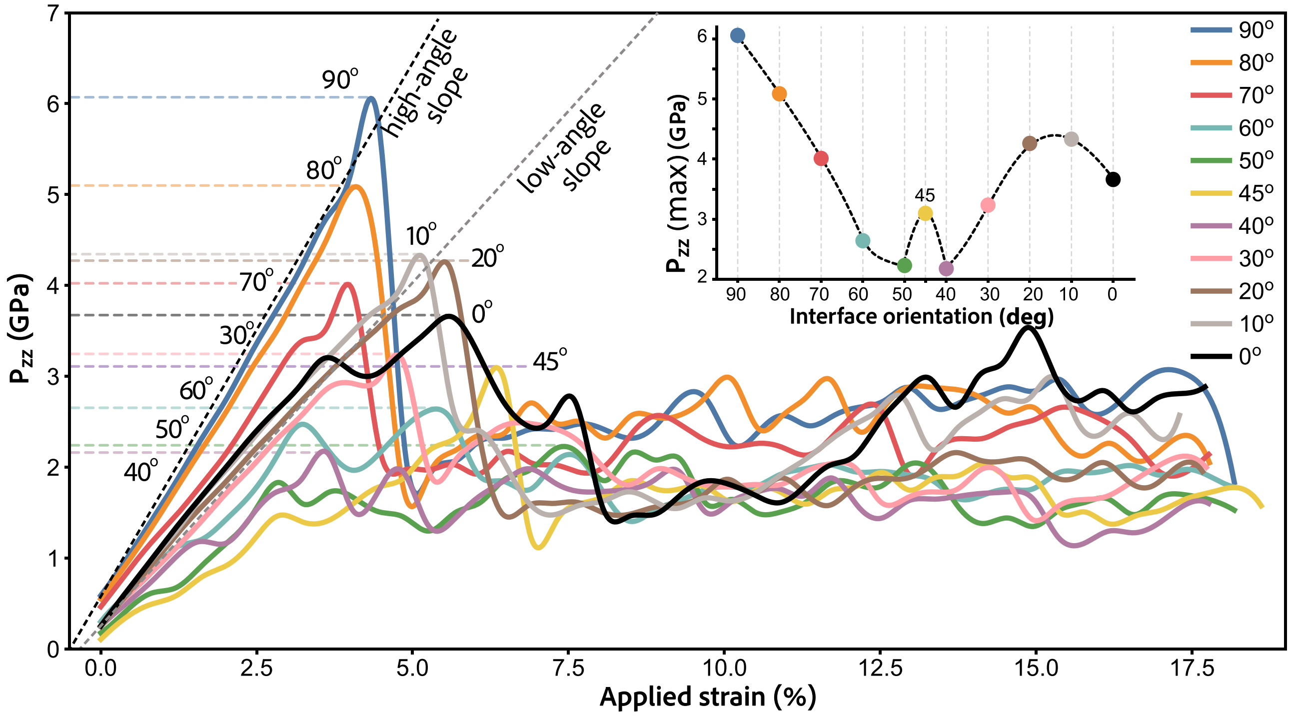

FIG. 6. Stress–strain response for Al/Ti flat interfaces as a function of interface rotation angle. Line plots are spline fits to the calculated stress values for visual clarity. The inset shows the change in peak stress with rotation.

dependence can be summarized as a transition between deformation regimes. At 90°, the response is Al-dominated, similar to the flat-interface case. At 80°−60°, the inclined interface promotes sliding, which lowers the peak stress and suppresses twinning. Near 45°, interface/slab alignment favors localization and bending. At 30°−10°, the dominant accommodation shifts into Ti through stacking faults, twinning, and, for some angles, hcp-to-fcc transformation. At 0°, early Al activity is followed by significant Ti twinning. A schematic summarizing the deformation mechanism with interface rotation is shown in Fig. 7.

The rotation of the bimetal microstructure changes the orientation of Ti and Al relative to the loading direction, as shown in Fig. 8. At 80° rotation, the mushrooming of Al begins earlier than in the 90° case (1.22% strain). Dislocation nucleation occurs at a similar strain as 90°, but the total dislocation density is significantly lower because the inclined interface facilitates sliding. At 1.22% applied strain, the calculated atomic shear strain indicates initial interface deformation by sliding; no dislocations are detected at this strain. The stress-strain profile at 80° rotation is similar to that of the flat interface (90° rotation), but with a reduced peak stress (Table II). At 80° rotation, Shockley partials are the dominant dislocations, followed by stair-rod dislocations, as shown in Fig. S13 [48]. In contrast to the flat interface, the rotated microstructure exhibits significant fluctuations in dislocation density due to strain accumulation at the interface that promotes sliding rather than dislocation-mediated plasticity [Fig. 9(a)]. Mushrooming is asymmetric relative to the flat interface, attributable to interface sliding. More pronounced sliding is observed on the right-hand side of Al at 14.2% strain (Fig. 8). Overall, the change in interface orientation promotes interface sliding, reduces the peak stress, shifts the initial deformation mechanism toward sliding before dislocation activity, suppresses twinning, and makes Al mushrooming asymmetric.

Furthermore, similar to the 80° rotation, for rotations up to 60°, the sliding of the interface occurs first (∼1.22% of applied strain), followed by dislocation nucleation. Figure 9(b) also shows that with reduced rotation and accompanying interface sliding, the strain required for dislocation nucleation decreases, indicating an easier onset of plasticity.

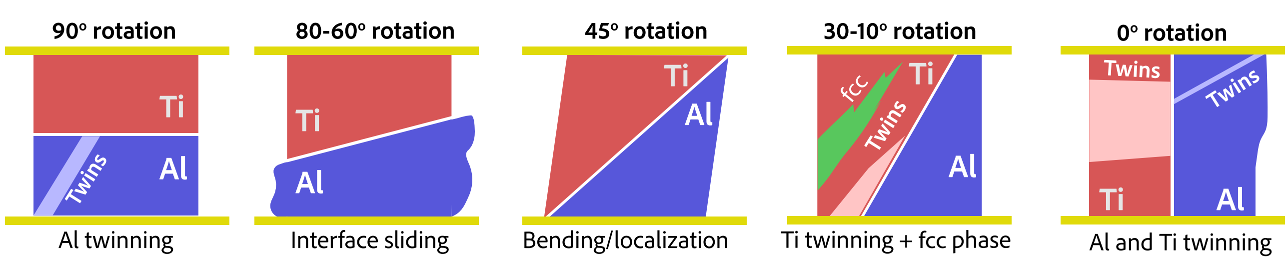

FIG. 7. Illustration of the deformation mechanism associated with interface rotation.

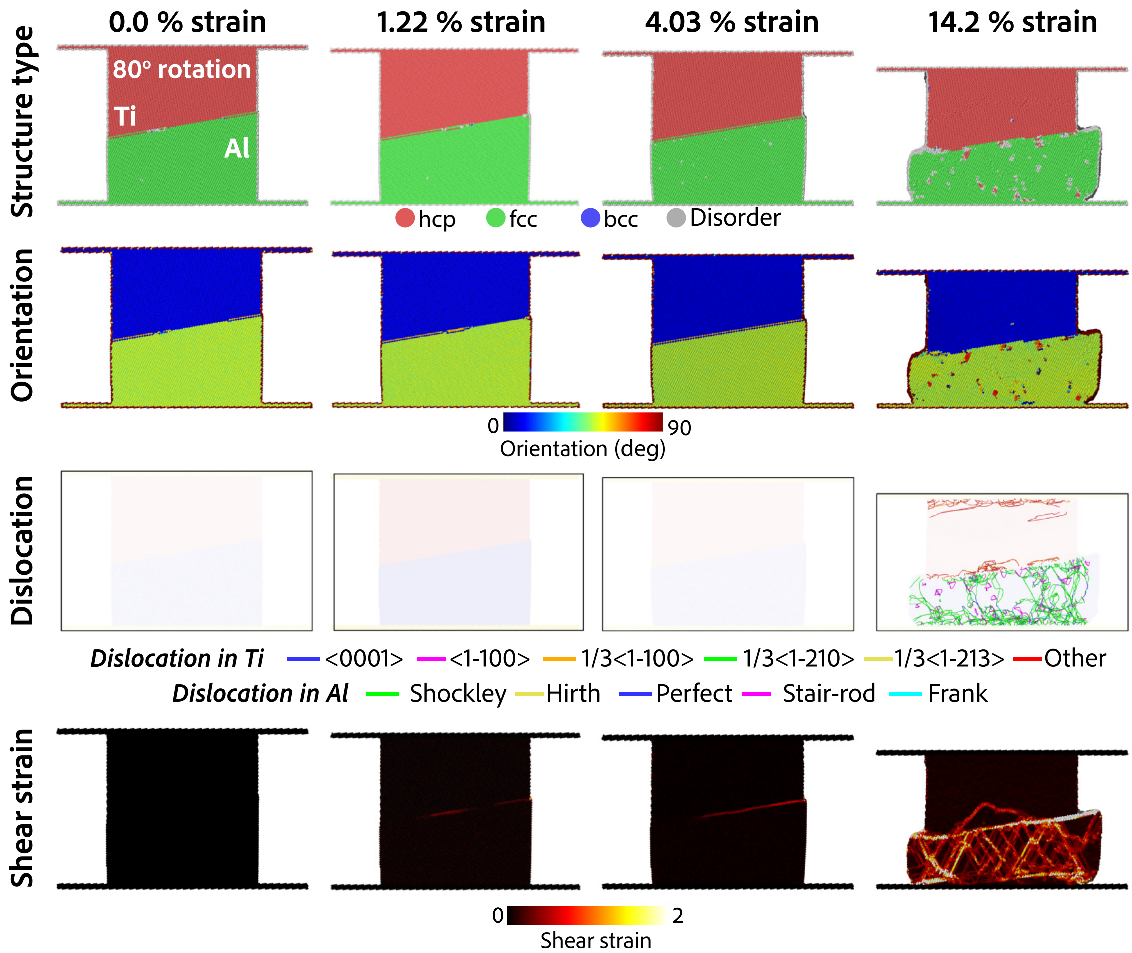

FIG. 8. Evolution of structure type, orientation, dislocations, and shear strain for 80° interface rotation at four different applied strains.

Interestingly, as the rotation decreases below 60°, dislocations are also observed in Ti even during the initial deformation [Fig. 9(a)]. These initial dislocations also cause orientation changes in Ti, which increase with applied strain. Another notable aspect is that with rotation, dislocations in Al are observed only in the lower region. In addition, deformation of Al under rotation shows that the metal is divided into two distinct regions approximately at the midthickness of the Al layer (consistent with the strain and temperature conditions reported), as shown in Fig. S14 [48] at 8.5% applied strain. Specifically, a significant increase in dislocation density is observed in the lower part of Al due to compression from the bottom slab, while the upper region near the interface shows almost no dislocations. This results from interface sliding and

TABLE II. Peak compressive stress (P_{zz}(max)) and strain (ε) at P_{zz}(max) for flat vs cosine interfaces ($a = 60$ Å, $f = 3$) at various rotations. Strain (ε) at P_{zz}(max).

	Flat interface		Cosine interface ($a = 60$ Å, $f = 3$)	
Rotation (deg)	P_{ZZ}(max) (GPa)	Strain (ε) at P_{zz}(max)	P_{zz}(max) (GPa)	Strain (ε) at P_{zz}(max)
90	5.81	4.50%	3.15	5.67%
80	5.07	4.03%	3.18	4.45%
70	3.93	4.05%	2.83	3.64%
60	2.62	5.24%	2.30	4.44%
50	2.20	7.28%	2.22	5.60%
45	2.94	6.48%	2.13	4.42%
40	2.16	3.63%	1.90	4.41%
30	3.16	4.85%	2.25	4.85%
20	4.18	5.60%	2.49	3.34%
10	4.22	5.22%	2.72	3.24%
0	3.66	5.62%	2.77	3.62%

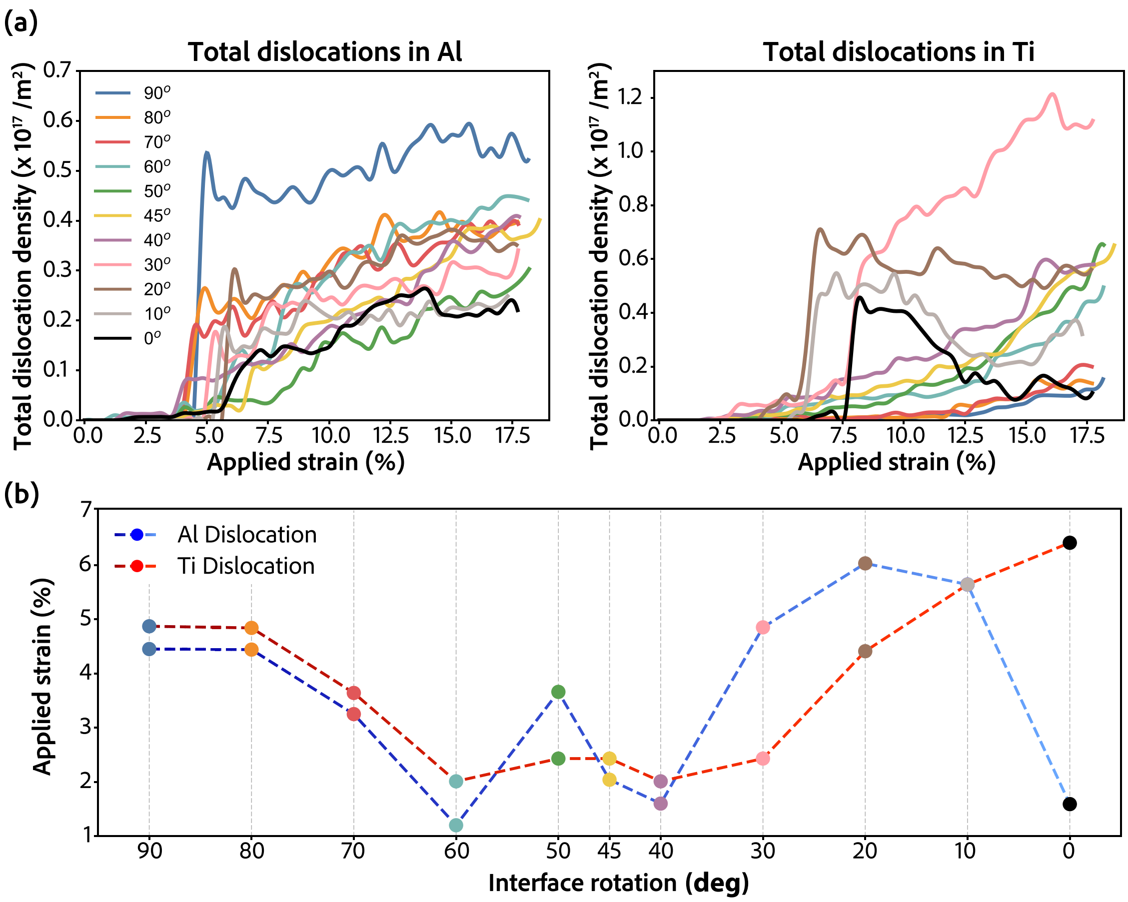

FIG. 9. (a) Evolution of total dislocation density as a function of interface rotation; lines are spline fits to the calculated dislocation-density values. (b) Applied strain (%) at which the first dislocation is observed in Al and Ti as a function of interface rotation.

deformation in Ti that accommodate the applied stress, reducing the total dislocation density in Al for rotations down to 60°. As the rotation decreases further to 45°, some dislocation nucleation is also observed at lower strain (2.43% strain), as shown in Fig. 10. However, at peak stress (6.48% strain) these dislocations remain localized at the interface, indicating that deformation is primarily controlled by interfaces over plastic flow. At 45° rotation, due to the nearly perfect alignment of the metals with the compression slabs, deformation is accommodated by the interface, and bending of the pillar is observed rather than mushrooming (Fig. 10). During the later stage of deformation (15.4% strain), Al shows two distinct regions, the same as in the 60° rotation case.

As the rotation angle decreases, the yield strain (strain at peak stress) increases relative to the flat interface and reaches a maximum at 50°, even as the peak stress decreases, as mentioned in Table II. Below 40° rotation, the response changes again: peak stress increases, and the corresponding strain exceeds that of the flat interface (Table II and Fig. 6). After peaking at 10°, the peak stress decreases at 0°, and the stress-strain response deviates slightly from the behavior between 20° and 30°. The microstructural characterization at 30° rotation shows that dislocations first nucleate in Ti at 3.25% strain and grow into stacking faults (SFs) at 5.28% strain, which serve as a precursor to twin nucleation (Fig. 11). Additionally, a phase transformation from the hcp to the fcc phase in Ti is observed at higher strain (>8%). This metastable hcp → fcc transition has been reported both experimentally and in atomistic modeling under extreme stress states [52–55], including cryogenic plane-strain compression of bulk Ti [52] and room-temperature compression of sub-micron Ti pillars [53], where TEM identifies thin fcc lamellae obeying prismatic/basal orientation relationships with the hcp matrix. The high resolved shear stresses under compression promote the basal/prismatic activity leading to the phase transformation. In the present nucleation-controlled regime, the hcp → fcc transition is preceded by Ti dislocation activity that develops into stacking faults, and the fcc region appears at higher strain and then grows with continued compression. This is consistent with the orientation relationship between hcp and fcc phases in hcp metals (they only differ by their stacking sequence), such that thickening of stacking faults can convert hcp stacking into fcc. In addition, our results show that Ti twinning nucleates adjacent to the phase-transformed region and evolves with the fcc fraction during deformation, consistent with TEM experiments. Given the high strain rate used here (10^8 s^{-1}), this comparison is intended to support the mechanistic pathway in modeling.

The phase-transformed fcc region grows, and additional SFs are observed in the upper part of Ti. Meanwhile, in Al, dislocations are observed in the top corner—opposite to the case at 40°−45° rotation, where they occur at the bottom corner. Later, the first twins are observed in Ti between the interface and the phase-transformed region at around 8% strain

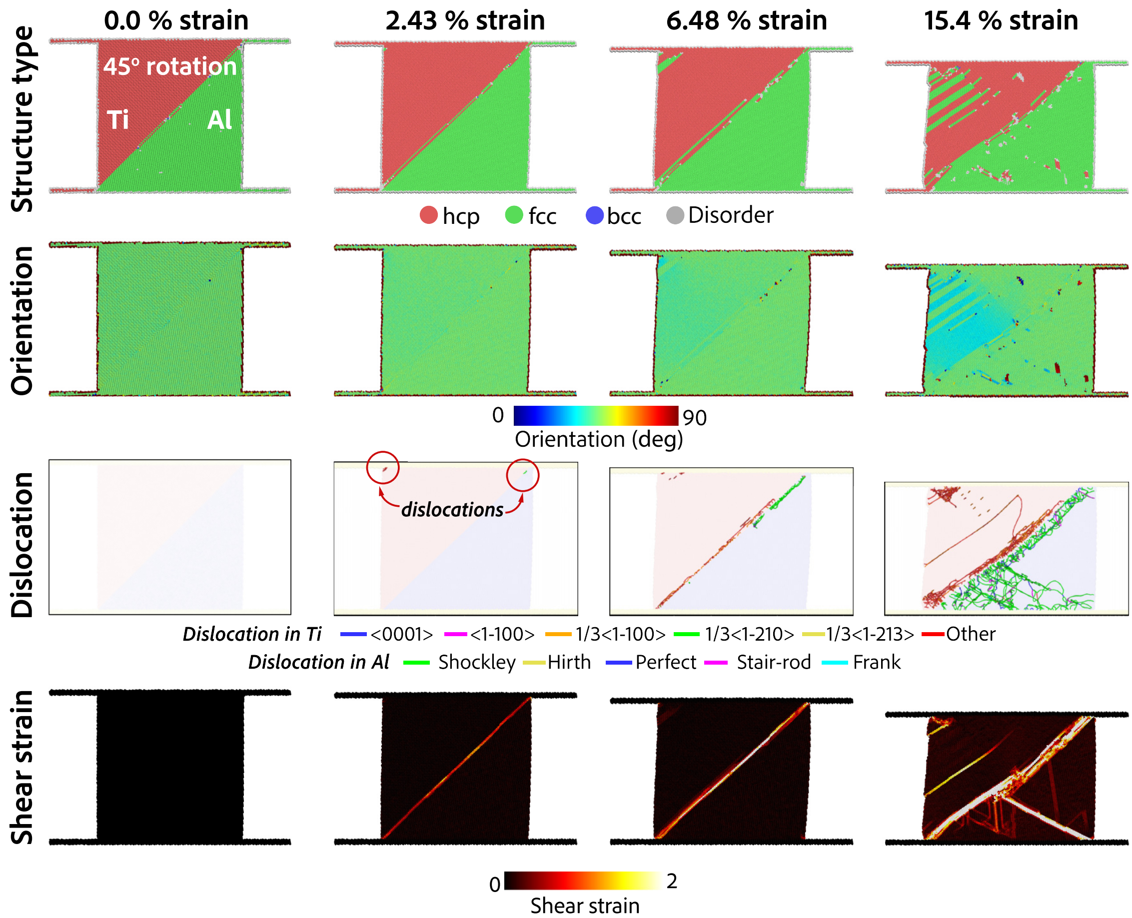

FIG. 10. Evolution of structure type, orientation, dislocations, and shear strain for 45° interface rotation at four different applied strains.

(Fig. 11). This twinning markedly increases the dislocation density in Ti, and additional dislocations form in the lower part of Al (Figs. 9 and S13 [48]). With further compression, the twin, the phase-transformed region, and the SFs in Ti continue to grow. However, due to buckling (without mushrooming) in Ti, the twin does not propagate toward the top of the microstructure, leading to rotation in the upper region of Ti, as shown in Fig. 11 at 14.1% strain. Sliding and buckling are also observed in the lower part of Ti, with an increasing twin volume fraction. Continued compression further enlarges the twin region, promotes additional phase transformation, and increases dislocation density in Ti, whereas the dislocation density in Al rises more slowly. Therefore, early plasticity is accommodated through Ti stacking faults, twinning, and phase transformation rather than extensive deformation of Al.

For 20° and 10° rotations, the stress-strain responses are similar, with peak stresses of 4.18 and 4.22 GPa, respectively. These are the highest peak stresses among rotations $<80°$ excluding 45°. The 0° case shows a lower peak. At 20°, the initial plasticity begins with nucleation of SFs in Ti—first in the upper region (close to the top slab), then in the lower. A twin forms at the center of Ti with little SF growth at 6.04% strain (Fig. S15 [48]). This twin variant differs from the 40° case. Twin nucleation in Ti, together with dislocations in both Ti and Al, reduces the peak stress compared to the 90° rotation. However, the peak remains elevated relative to most other angles because the early dislocation density in Ti is higher and buckling is stronger. Meanwhile, dislocations in Al are distributed throughout the region. Subsequently, another twin variant appears in Ti—similar to the 40° case—while the dislocation density in Ti increases during the initial deformation (in contrast to the 40° rotation). With further deformation in the 20° microstructure, the first twin variant disappears while the second grows from the bottom of Ti. Dislocations in Al remain steady, whereas dislocations decrease in Ti due to annihilation associated with the first twin variant, leaving no dislocations around the twin region. In contrast, as the twin volume fraction for the second twin variant increases, the twin surface area decreases; hence, the dislocation density is reduced. At higher strains (∼13%), additional phase-transformed fcc Ti forms, further reducing the dislocation density, as shown in Fig. S15 [48]. Unlike the 90° (flat-interface) case, prominent mushrooming is observed in Ti. With continued deformation, the twin becomes the dominant phase in Ti, while the original Ti phase diminishes and becomes confined near the top compression slab (Fig. S15 [48]).

For the 10° interface rotation, the stress–strain response is similar to that of the 20° rotation and shows combined deformation of Al and Ti (Fig. 6). Compression of Ti leads to the formation of a twin region, with the orientation angle changing from ∼80° to 6°–10° at ∼6.6% applied strain, as shown in Fig. S16 [48]. The precursor to this twin is dislocation activity in Ti and deformation at the Ti corner.

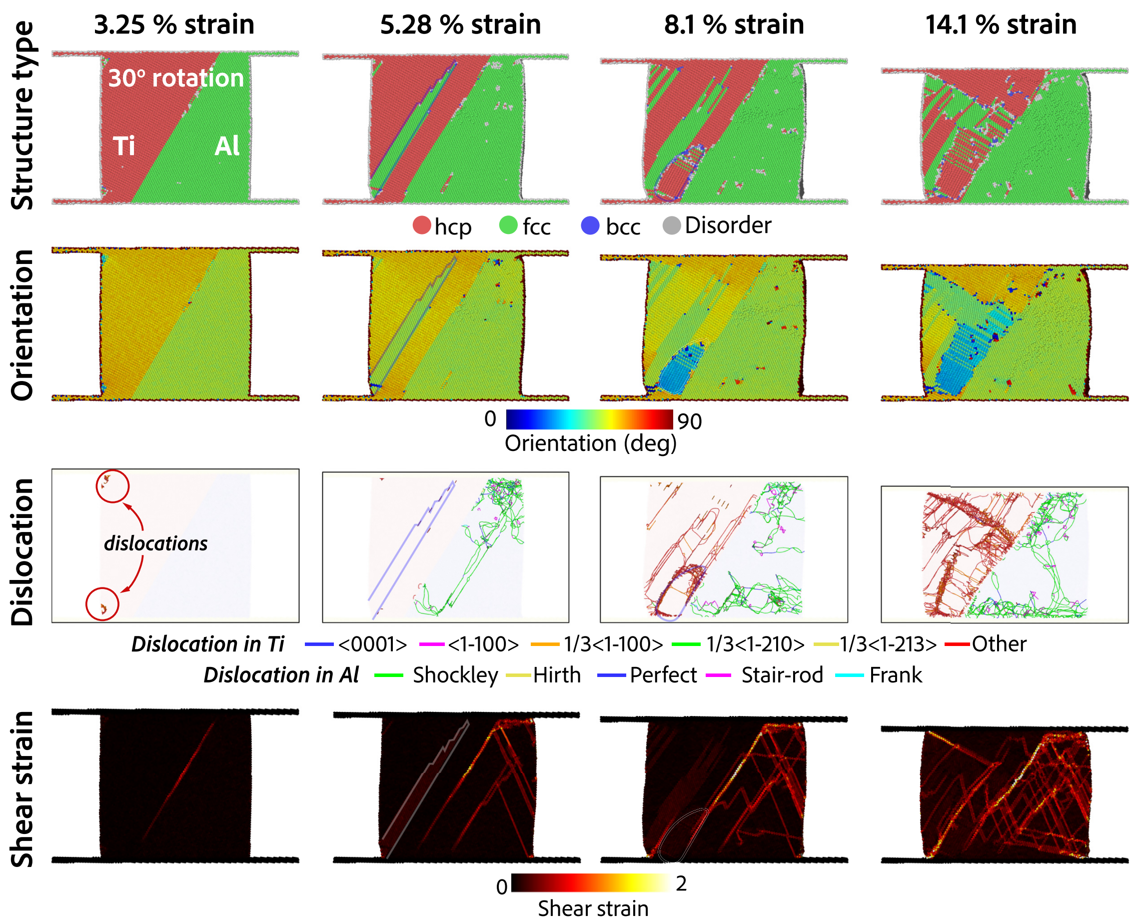

FIG. 11. Evolution of structure type, orientation, dislocations, and shear strain for 30° interface rotation at four different applied strains.

As deformation increases, the twin grows toward the upper compression slab. Notably, neither stacking faults (SFs) nor a phase-transformed fcc Ti is present, unlike in the $\sim 30^\circ$ rotation case. As Fig. 9 shows, dislocation nucleation in Al and Ti occurs at the same strain value, just after the peak compressive stress, indicating that the onset of plasticity is shared by both metals. Dislocations in Al are distributed (Fig. S16 [48]) because both slabs compress these regions nearly vertically, while dislocations in Ti are located around the twin region along the inclined incoherent twin boundary. Hence, a reduction in the incoherent twin region leads to a decrease in dislocation density. The increase in twin volume fraction, reduces the incoherent part of the twin region. In addition, no evidence of a phase-transformed fcc Ti phase is observed at higher strains ($>10\%$). Therefore, there is no contribution from phase transformation during deformation, leading to a reduced dislocation density in Ti at higher strain. For the 20° rotation, the reduction in dislocation density is due to the annihilation of one twin variant and the growth of the other. However, due to the presence of fcc Ti, more dislocations are observed at higher strain for the 20° rotation than for the 10° rotation. For the 10° rotation, the dislocation density in Al is less than that in the 30° and 20° rotations because deformation is nearly vertical. At higher strains, there is no evidence that the original Ti matrix remains (Fig. S16 [48]).

In the case of 0° rotation, deformation begins with the nucleation of a dislocation in the top region of Al, which travels toward the interface. Upon reaching the interface, this initial dislocation in Al triggers the formation of a thin twin region. After the peak stress, the amount of dislocations in Al increases, and the twin fraction decreases, as shown in Fig. 12. Buckling (without mushrooming) in Al begins at the top region and progresses toward the bottom, resembling the behavior observed at 90° rotation. Meanwhile, a small amount of dislocations are observed in Ti at 5.28%. With further deformation, a significant number of twins are introduced in Ti, consistent with the twin variant observed at $\geqslant 30^\circ$ rotation. This twinning leads to substantial buckling of Ti in the top region at approximately 8% strain, as shown in Fig. 12, which results in a marked stress reduction. As this twin variant grows, the dislocation density in Ti decreases, reaching the lowest value in the $0^\circ - 30^\circ$ rotation range. Meanwhile, the dislocation density in Al remains similar to earlier rotations. Overall, deformation across different interface rotations underscores the role of macroscopic degrees of freedom arising from changes in the Schmid factors for Al and Ti and from the rotation of the interface relative to the loading direction. Therefore, rotation changes the resolved shear stresses in Al and Ti (activating different slip systems during deformation), compatibility between the interface and the loading direction, and whether strain is accommodated by bulk

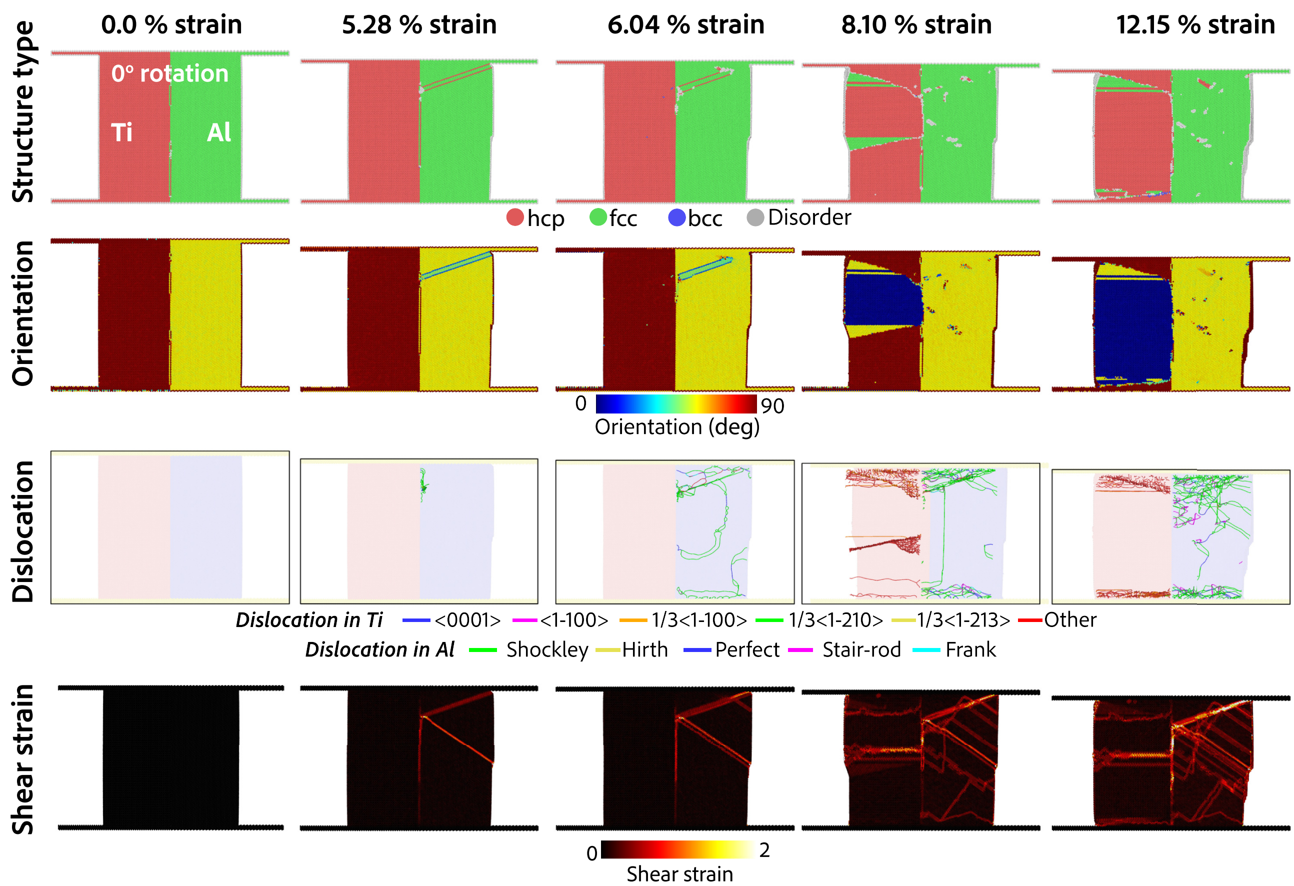

FIG. 12. Evolution of structure type, orientation, dislocations, and shear strain for 0° interface rotation at four different applied strains.

plasticity or by interfacial localization. These coupled changes explain the modified initial stress–strain slope reflecting the system's stiffness and its resistance to deformation under loading (Figs. 6 and 9). Moreover, the variation in peak stress with rotation reflects a mechanism shift in the intermediate range, from deformation in Al to sliding at the interface. At lower rotation, Ti stacking-fault activity, twinning, and phase transformation become the dominant mechanism. Therefore, interface rotation should be interpreted as a mechanism map that changes between Al-dominated, interface-dominated, and Ti-dominated deformation modes.

D. Roughness and rotation

To examine which factor dominates—the macroscopic degrees of freedom due to rotation or the microscopic behavior due to modifications in interface roughness (waveform interfaces)—simulations are conducted for a cosine interface with an amplitude $a = 60$ Å and a frequency $f \approx 3$ at various interface rotation angles. The frequency is approximate because the model is first constructed with $f = 5$, then rotated to the desired angle and cropped to maintain fixed cell dimensions and periodic boundary conditions, which changes the projected wavelength along the interface and yields an effective $f \approx 3$. Achieving exactly $f = 3$ with this workflow is difficult; it would require selecting a different initial f, applying a specific rotation, and cropping so that an integer number of wavelengths fits the domain without lattice mismatch. To avoid these complications, $f \approx 3$ is used. This accounts for the deviation observed in the stress–strain profile for the cosine interface at 90° rotation (Table II) and for differences noted in the roughness section (Fig. 13). However, the deformation mechanism (including mushrooming) remains similar. For bimetals with rotated cosine interfaces, the peak stress decreases as rotation is reduced from 90° toward 40°, then increases again as the angle approaches 0°, as shown in Fig. 13. Twinning in Ti is still observed under rotation, indicating that the dominant deformation mechanism persists, while its activity is modulated by angle. Figure 13 shows comparative stress–strain curves for flat and cosine interfaces across rotation. With rotation, the peak stress for the flat interface remains higher than that for the cosine interface; however, the difference is smaller for rotations between 60° and 40°. In addition, the Ti sliding at the interface observed for flat interfaces between 30° and 45° is significantly reduced in the cosine cases due to geometric locking by the waveform interface pattern. Thus, maintaining similar early deformation while avoiding Ti sliding helps keep the peak stress close to that of the flat interface in the 30°–50° range. This indicates that the macroscopic response is overall dominated over microscopic behavior, with competition between scales in some cases. Roughness mainly lowers the stress for initial interfacial activation, whereas rotation determines which deformation mechanism is favored. Their interaction

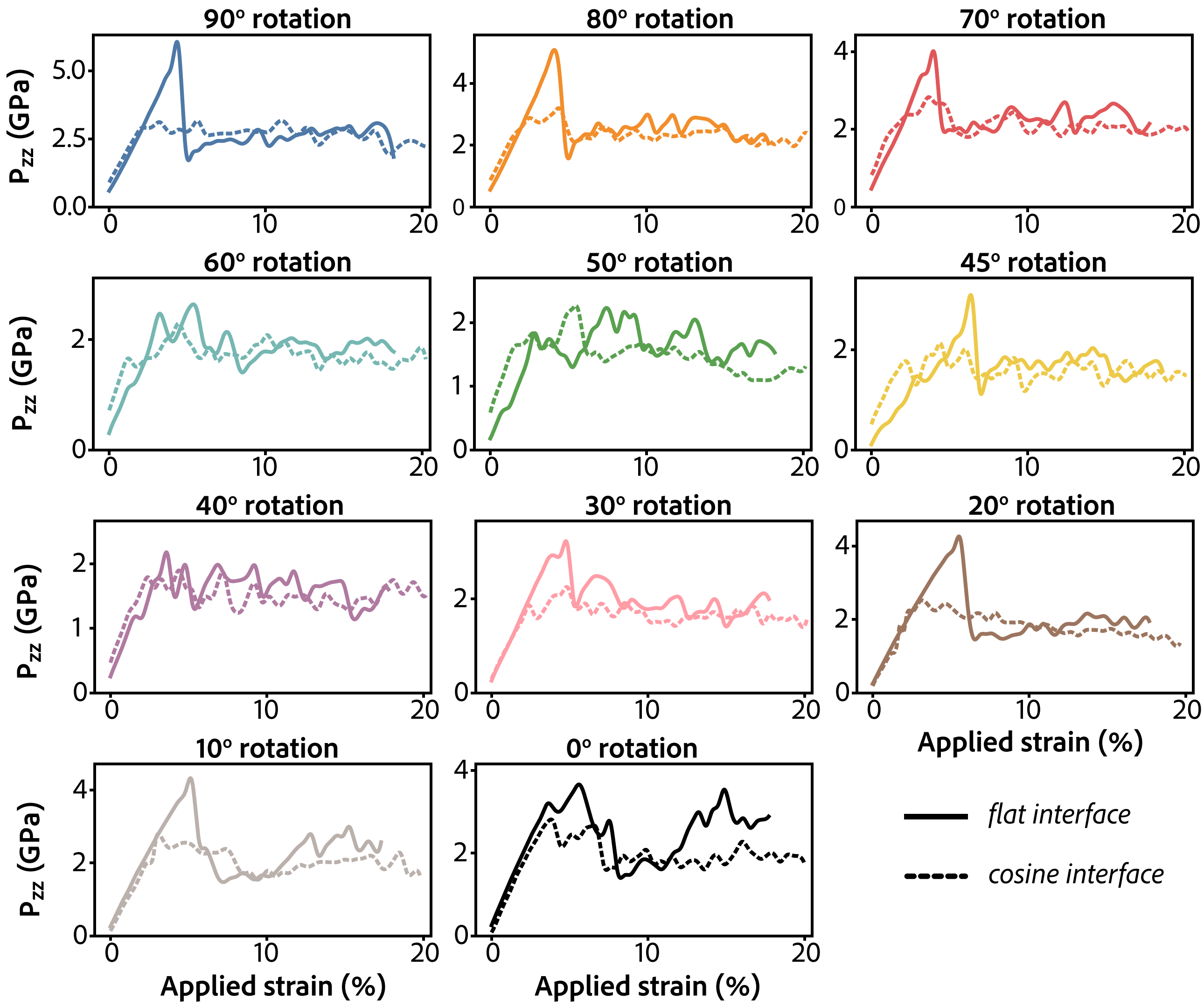

FIG. 13. Stress-strain response under uniaxial compression of Al/Ti flat and cosine interfaces ($a = 60$ Å, $f \sim 3$) bimetals across interface rotations. The line plots are splines fitted to the calculated stress values.

is most evident between about 30°–50°, where the cosine morphology geometrically limits the extensive sliding.

IV. CONCLUSION

In summary, the role of interface roughness and interface rotation, corresponding to microscopic and macroscopic degrees of freedom, respectively, was investigated in Al/Ti bimetals under high-strain-rate uniaxial compression. Although the waveform and rotated interfaces considered here are idealized, they represent simplified surrogates for experimentally relevant interface states in Al/Ti bimetals. Interface roughness lowers the stress required for plasticity activation and shifts the response toward interface-assisted deformation due to the presence of preexisting dislocations and stress concentrations at the interface. For the square interface, the step height acts as a geometric parameter, separating locally flat regions and influencing the onset of dislocation nucleation. The study also highlights the importance of waveform frequency, which modifies microscopic degrees of freedom at the interface and thereby affects the initiation of plasticity through changes in the local atomic arrangement. Interface rotation changes the dominant deformation mechanism from Al twinning in the high-rotation case to interface sliding, localization, and pillar bending at intermediate rotations, and finally to stacking-fault-mediated Ti twinning with fcc phase transformation, or Ti twinning alone, at lower rotations. The combined roughness-plus-rotation results further show that waveform interfaces can geometrically limit sliding in inclined interfaces while still retaining lower activation stresses than flat interfaces. Overall, the study underscores that interface roughness and rotation are effective design variables that control both the stress required for plasticity initiation and the dominant deformation mechanism in Al/Ti bimetals. These trends provide useful guidance for designing lightweight structural materials for applications under extreme loading conditions.

ACKNOWLEDGMENTS

Simulations utilized resources provided by the LANL Institutional Computing Program. The work was performed as a component of LDRD Project No. 20230128DR. This work was supported by the U.S. Department of Energy through the Los Alamos National Laboratory. Los Alamos National Laboratory is operated by Triad National Security, LLC, for the National Nuclear Security Administration of the U.S. Department of Energy (Contract No. 89233218CNA000001).

DATA AVAILABILITY

The data that support the findings of this article are not publicly available upon publication because it is not technically feasible and/or the cost of preparing, depositing, and hosting the data would be prohibitive within the terms of this research project. The data are available from the authors upon reasonable request.

[1] I. J. Beyerlein and J. Wang, Interface-driven mechanisms in cubic/noncubic nanolaminates at different scales, MRS Bull. **44**, 31 (2019).

[2] W. Z. Han, E. K. Cerreta, N. A. Mara, I. J. Beyerlein, J. S. Carpenter, S. J. Zheng, C. P. Trujillo, P. O. Dickerson, and A. Misra, Deformation and failure of shocked bulk Cu-Nb nanolaminates, Acta Mater. **63**, 150 (2014).

[3] S. J. Fensin, E. K. Walker, E. K. Cerreta, C. P. Trujillo, D. T. Martinez, and G. T. Gray, Dynamic failure in two-phase materials, J. Appl. Phys. **118**, 235305 (2015).

[4] X. Shen, B. Yao, Z. Liu, D. Legut, H. Zhang, and R. Zhang, Mechanistic insights into interface-facilitated dislocation nucleation and phase transformation at semicoherent bimetal interfaces, Int. J. Plast. **146**, 103105 (2021).

[5] S. J. Fensin, E. K. Walker, E. K. Cerreta, and G. T. Gray III, When do interfaces become important for failure? EPJ Web Conf. **94**, 02010 (2015).

[6] A. Mishra, J. Lind, M. Kumar, and A. M. Dongare, Understanding the phase transformation mechanisms that affect the dynamic response of Fe-based microstructures at the atomic scales, J. Appl. Phys. **130**, 215902 (2021).

[7] N. Beets, Y. Cui, D. Farkas, and A. Misra, Mechanical response of a bicontinuous copper-molybdenum nanocomposite: Experiments and simulations, Acta Mater. **178**, 79 (2019).

[8] A. Selimov, K. Chu, and D. McDowell, Effects of interdiffusion on shear response of semi-coherent {111} interfaces in Ni/Cu, Int. J. Plast. **157**, 103393 (2022).

[9] C. Wang, B. Yao, Z. Liu, X. Kong, D. Legut, R. Zhang, and Y. Deng, Effects of solutes on dislocation nucleation and interface sliding of bimetal semi-coherent interface, Int. J. Plast. **131**, 102725 (2020).

[10] M. J. Echeverria, S. Galitskiy, A. Mishra, R. Dingreville, and A. M. Dongare, Understanding the plasticity contributions during laser-shock loading and spall failure of Cu microstructures at the atomic scales, Comput. Mater. Sci. **198**, 110668 (2021).

[11] Y. Zhang, Z. Liu, B. Yao, D. Legut, and R. Zhang, Atomic insights into interface-mediated plasticity and engineering principles for heterogeneous serrated interfaces, Int. J. Plast. **160**, 103498 (2023).

[12] J. Chen, S. N. Mathaudhu, N. Thadhani, and A. M. Dongare, Unraveling the role of interfaces on the spall failure of Cu/Ta multilayered systems, Sci. Rep. **10**, 208 (2020).

[13] S. Shu, X. Zhang, J. A. Beach, P. Bellon, and R. S. Averback, Irradiation-induced formation of nanorod precipitates in a dilute Cu-W alloy, Scr. Mater. **115**, 155 (2016).

[14] I. Beyerlein, M. Demkowicz, A. Misra, and B. Uberuaga, Defect-interface interactions, Prog. Mater. Sci. **74**, 125 (2015).

[15] J. Chen, M. A. Tschopp, and A. M. Dongare, Role of nanoscale Cu/Ta interfaces on the shock compression and spall failure of nanocrystalline Cu/Ta systems at the atomic scales, J. Mater. Sci. **53**, 5745 (2018).

[16] A. Mishra, M. J. Echeverria, K. Ma, S. Parida, C. Chen, S. Galitskiy, and A. M. Dongare, Virtual texture analysis to investigate the deformation mechanisms in metal microstructures at the atomic scale, J. Mater. Sci. **57**, 10549 (2022).

[17] A. Mishra, C. Kunka, M. J. Echeverria, R. Dingreville, and A. M. Dongare, Fingerprinting shock-induced deformations via diffraction, Sci. Rep. **11**, 9872 (2021).

[18] G. Kurdjumow and G. Sachs, Über den mechanismus der stahlhärtung, Z. Phys. **64**, 325 (1930).

[19] L. Sandoval, H. M. Urbassek, and P. Entel, The Bain versus Nishiyama-Wassermann path in the martensitic transformation of Fe, New J. Phys. **11**, 103027 (2009).

[20] S. Zheng, J. S. Carpenter, R. J. McCabe, I. J. Beyerlein, and N. A. Mara, Engineering interface structures and thermal stabilities via SPD processing in bulk nanostructured metals, Sci. Rep. **4**, 4226 (2014).

[21] A. Thyagatur and L. T. Mushongera, Effect of interface orientation and loading direction on the mechanical response of Cu-Nb multilayered nanocomposites, J. Mater. Eng. Perform. **32**, 3371 (2023).

[22] A. Thyagatur and L. T. Mushongera, Unraveling the effects of interface orientation and crystallography on the deformation mechanisms of accumulative roll-bonded Cu-Nb–multilayered nanocomposites using molecular dynamics, J. Mol. Model. **28**, 166 (2022).

[23] A. Afrouzian and A. Bandyopadhyay, Understanding the role of interface in deformation behavior of additively manufactured bimetallic structures of pure metals, J. Mater. Res. Technol. **30**, 70 (2024).

[24] S. Ziaei, Q. Wu, and M. A. Zikry, Orientation relationships between coherent interfaces in hcp–fcc systems subjected to high strain-rate deformation and fracture modes, J. Mater. Res. **30**, 2348 (2015).

[25] N. Fuchs-Lynch, M. De Leo, P. Garg, S. Xu, N. A. Mara, and I. J. Beyerlein, 3D interface size effects on slip transfer in Ti/Nb nanolaminates, Int. J. Plast. **186**, 104246 (2025).

[26] H. Zhang, X. Ou, S. Ni, H. Yan, X. Liao, and M. Song, Atomic-scale study of the $\{11\bar{2}1\}$ twinning and $\{11\bar{2}2\}-\{11\bar{2}1\}$ double twinning mechanisms in pure titanium, Int. J. Plast. **160**, 103486 (2023).

[27] B. Wang, W. Zeng, Z. Zhao, R. Jia, J. Xu, and Q. Wang, Near-α titanium alloy dwell load-induced deformation twinning to coordinate the deformation mechanism associated with crack initiation, Int. J. Plast. **182**, 104116 (2024).

[28] Q. Yang, Y. Yang, B. Wang, Y. Guo, and X. Chen, Molecular dynamics study on the multi-spallation of Ti-6Al-4V titanium alloy caused by non-planar effect of shock wave induced by microscopic interface, Int. J. Plast. **196**, 104542 (2025).

[29] Q. Huang, Q. Zhao, H. Zhou, and W. Yang, Misorientation-dependent transition between grain boundary migration and sliding in FCC metals, Int. J. Plast. **159**, 103466 (2022).

[30] R. Kumar, J. Chen, A. Mishra, and A. M. Dongare, Interface microstructure effects on dynamic failure behavior of layered Cu/Ta microstructures, Sci. Rep. **13**, 11365 (2023).

[31] Y. Cui, D. Liu, M. Fan, G. Deng, L. Sun, Y. Zhang, D. Chen, and Z. Zhang, Microstructure and mechanical properties of TA1/3A21 composite plate fabricated via explosive welding, Mater. Sci. Technol. **36**, 425 (2020).

[32] G. Agarwal and A. M. Dongare, Shock wave propagation and spall failure in single crystal Mg at atomic scales, J. Appl. Phys. **119**, 145901 (2016).

[33] C. Chen, S. Galitskiy, A. Mishra, and A. M. Dongare, Modeling laser interactions with aluminum and tantalum targets using a hybrid atomistic-continuum model, J. Appl. Phys. **133**, 105901 (2023).

[34] S. Galitskiy, A. Mishra, and A. M. Dongare, Modeling shock-induced void collapse in single-crystal Ta systems at the mesoscales, Int. J. Plast. **164**, 103596 (2023).

[35] M. Xiang, Y. Liao, K. Wang, G. Lu, and J. Chen, Shock-induced plasticity in semi-coherent {111} Cu-Ni multilayers, Int. J. Plast. **103**, 23 (2018).

[36] J. Huang, M. Lei, G. Yang, and B. Wen, Twinning induced by asymmetric shear response, Int. J. Plast. **185**, 104226 (2025).

[37] J. Zhang, L. Qian, W. Yang, J. Wang, and X.-S. Yang, Dislocation nucleation and shear sliding at dual-phase high-entropy alloy semi-coherent interface with atomic complexity, Acta Mater. **293**, 121118 (2025).

[38] Z. Nishiyama, *Martensitic Transformation* (Elsevier, 2012).

[39] M. R. An, H. Y. Song, Q. Deng, M. J. Su, and Y. M. Liu, Influence of interface with mismatch dislocations on mechanical properties of Ti/Al nanolaminate, J. Appl. Phys. **125**, 165307 (2019).

[40] Z. Ma, Y. Jin, S. Ji, X. Meng, L. Ma, and Q. Li, A general strategy for the reliable joining of Al/Ti dissimilar alloys via ultrasonic assisted friction stir welding, J. Mater. Sci. Technol. **35**, 94 (2019).

[41] H. Zhang, B. Wei, X. Ou, S. Ni, H. Yan, and M. Song, Atomic-level study of $\{10\bar{1}1\}$ deformation twinning in pure Ti and Ti-5at.% Al alloy, Int. J. Plast. **153**, 103273 (2022).

[42] H. Zhang, X. Li, J. Zhang, S. Li, S. Gao, G. Liu, and J. Sun, Manipulating the interfacial structures in titanium alloys containing interstitial solutes delivers ultra-high strength and ductility, Int. J. Plast. **187**, 104288 (2025).

[43] S. Wei, J. Kim, and C. C. Tasan, *In-situ* investigation of plasticity in a Ti-Al-V-Fe ($\alpha + \beta$) alloy: Slip mechanisms, strain localization, and partitioning, Int. J. Plast. **148**, 103131 (2022).

[44] S. Plimpton, Fast parallel algorithms for short-range molecular dynamics, J. Comput. Phys. **117**, 1 (1995).

[45] R. R. Zope and Y. Mishin, Interatomic potentials for atomistic simulations of the Ti-Al system, Phys. Rev. B **68**, 024102 (2003).

[46] S. Moon, J. H. Paek, Y. H. Jang, and K. Kang, Mixing behavior of Ti–Al interface during the ultrasonic welding process and its welding strength: Molecular dynamics study, Heliyon **10**, e25116 (2024).

[47] H. Guo, M. M. Zhang, D. S. Xu, J. H. Zhang, J. K. Qiu, Z. C. Meng, S. J. Zheng, Y. J. Ma, H. Wang, and R. Yang, Planar slip triggered by successive dislocation-precipitate interaction in titanium alloys, Mater. Sci. Eng. A **882**, 145468 (2023).

[48] See Supplemental Material at http://link.aps.org/supplemental/10.1103/44bt-jb3p for the details of equilibration prior to loading, stress calculations, various interface geometries, role of periodic lateral directions and frequency, the evolution of dislocation densities, and the microstructural evolution during deformation, which includes Refs. [56–63].

[49] A. Stukowski, Visualization and analysis of atomistic simulation data with OVITO–the open visualization tool, Modell. Simul. Mater. Sci. Eng. **18**, 015012 (2010).

[50] D. M. Fronczek, J. Wojewoda-Budka, R. Chulist, A. Sypien, A. Korneva, Z. Szulc, N. Schell, and P. Zieba, Structural properties of Ti/Al clads manufactured by explosive welding and annealing, Mater. Des. **91**, 80 (2016).

[51] S. J. Fensin, J. P. Escobedo-Diaz, C. Brandl, E. K. Cerreta, G. T. Gray, T. C. Germann, and S. M. Valone, Effect of loading direction on grain boundary failure under shock loading, Acta Mater. **64**, 113 (2014).

[52] D. Hong, T. Lee, S. Lim, W. Kim, and S. Hwang, Stress-induced hexagonal close-packed to face-centered cubic phase transformation in commercial-purity titanium under cryogenic plane-strain compression, Scr. Mater. **69**, 405 (2013).

[53] W. Kou, Q. Sun, L. Xiao, and J. Sun, Plastic deformation-induced HCP-to-FCC phase transformation in submicron-scale pure titanium pillars, J. Mater. Sci. **55**, 2193 (2020).

[54] J. X. Yang, H. L. Zhao, H. R. Gong, M. Song, and Q. Q. Ren, Proposed mechanism of HCP→ FCC phase transition in titianium through first principles calculation and experiments, Sci. Rep. **8**, 1992 (2018).

[55] Y. Ma, Y. Chen, X. Yu, B. Zhang, L. Wang, and Y. He, In situ TEM observation of HCP to FCC transitions in hexagonal close-packed titanium, Mater. Res. Lett. **12**, 956 (2024).

[56] A. Stukowski, V. V. Bulatov, and A. Arsenlis, Automated identification and indexing of dislocations in crystal interfaces, Modell. Simul. Mater. Sci. Eng. **20**, 085007 (2012).

[57] A. Stukowski and K. Albe, Extracting dislocations and non-dislocation crystal defects from atomistic simulation data, Modell. Simul. Mater. Sci. Eng. **18**, 085001 (2010).

[58] J. D. Honeycutt and H. C. Andersen, Molecular dynamics study of melting and freezing of small Lennard-Jones clusters, J. Phys. Chem. **91**, 4950 (1987).

[59] H. Tsuzuki, P. S. Branicio, and J. P. Rino, Structural characterization of deformed crystals by analysis of common atomic neighborhood, Comput. Phys. Commun. **177**, 518 (2007).

[60] P. M. Larsen, S. Schmidt, and J. Schiøtz, Robust structural identification via polyhedral template matching, Modelling Simul. Mater. Sci. Eng. **24**, 055007 (2016).

[61] C. L. Kelchner, S. J. Plimpton, and J. C. Hamilton, Dislocation nucleation and defect structure during surface indentation, Phys. Rev. B **58**, 11085 (1998).

[62] F. Shimizu, S. Ogata, and J. Li, Theory of shear banding in metallic glasses and molecular dynamics calculations, Mater. Trans. **48**, 2923 (2007).

[63] M. L. Falk and J. S. Langer, Dynamics of viscoplastic deformation in amorphous solids, Phys. Rev. E **57**, 7192 (1998).